Chapter IV

Results and Discussion

IV.1 Synthesis and Resolution of Biphenol Molecular Motor (M1)

In this research, the biphenol molecular motor (**M1**) was synthesized from its precursors and then separated into its enantiomers through resolution.

IV.1.1 Synthesis of biphenol molecular motor (M1)

The biphenol molecular motor (**M1**) was synthesized in three reaction steps. The retrosynthetic analysis of biphenol molecular motor (**M1**) is shown in **Figure IV.1**. The first step is the functional group interconversion in which hydroxyl group can be obtained from the deprotection of methoxy group. The central double bond in the bismethoxy molecular motor (**28**) is introduced by homocoupling of its corresponding indanone precursor (**27**). The indanone precursor (**27**) can be made from 2,5-dimethylanisole (**31**) and methacrylic acid (**32**) as the starting materials.

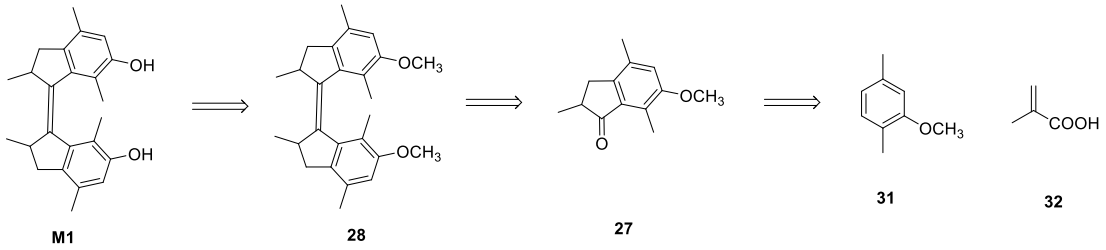

Figure IV.1 Retrosynthetic analysis of biphenol molecular motor (**M1**)

The first step in the synthesis of biphenol molecular motor (**M1**) is the Friedel-Crafts reaction between 2,5-dimethylanisole (**31**) and methacrylic acid (**32**) catalyzed by polyphosphoric acid (PPA) (**Figure IV.2**). This is a regioselective synthesis of indanone (**27**) as reported in the literature[81]. The regioselectivity of this reaction depends on the P_2O_5 content (76% or 83%) of the PPA. By employing PPA (76% P_2O_5), upon heating at 100 ℃ for 4 hours, the reaction went to full conversion and led to the formation of indanone (**27**) with the electron-donating group (-OCH_3) at *meta*

position to the carbonyl functionality in 59% yield. Indanone (**27**) was characterized by melting point determination, ^{1}H and ^{13}C NMR, as well as high resolution mass spectroscopy (HRMS) (see Experimental Section). All the characterization data corresponded to those previously reported in the literature[81].

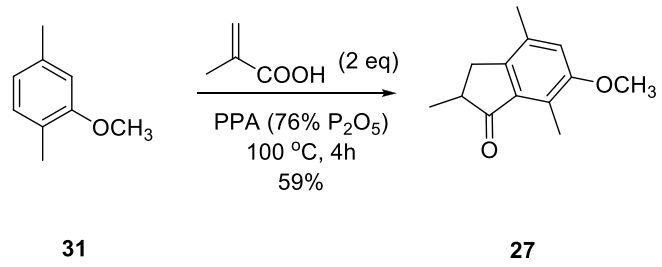

Figure IV.2 Synthesis of indanone precursor (**27**)

The proposed mechanism of this reaction is shown in **Figure IV.3**. A ^{31}P NMR experiment showed that the phosphoric anhydride of methacrylic acid (**32**) was not formed at low PPA concentration (76% P_2O_5)[81]. It is also proposed that the formation of acylium ion (**35**) is slower due to the lower acidity of the medium and the absence of the phosphorus anhydride. As a result, the arene (**31**) undergoes Friedel-Crafts alkylation in a 1,4-fashion with activated methacrylic acid (**34**) followed by subsequent intramolecular Friedel-Crafts acylation to give **27**[81].

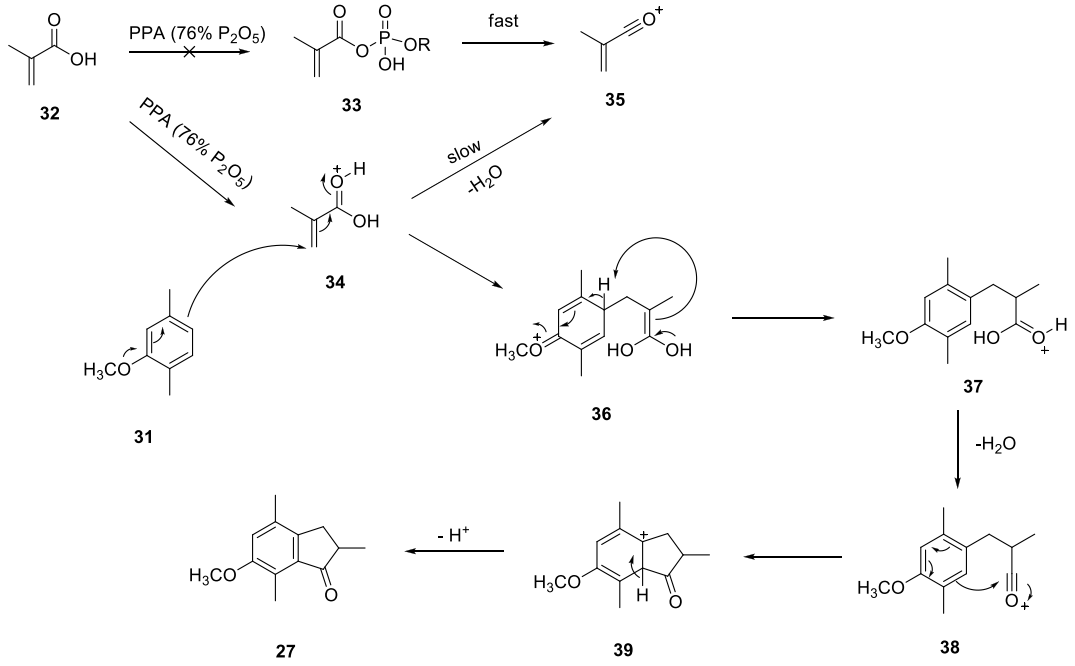

Figure IV.3 Proposed mechanism of the synthesis of indanone (**27**)

The second step is the McMurry homocoupling of the indanone precursor (**27**) to yield bismethoxy molecular motor (**28**) (**Figure IV.4**). This reaction was carried out using Zn powder and $TiCl_4$ in dry THF under N_2 atmosphere. At first, the mixture of Zn powder and $TiCl_4$ in dry THF was refluxed for 2 hours before adding the indanone precursor (**27**) to allow the formation of active Ti(II) species from $TiCl_4$ by means of reduction by Zn. Upon heating the reaction mixture at reflux for 5 days, the reaction went to full conversion and bismethoxy molecular motor (**28**) was obtained in 74% yield as a mixture of *E* and *Z* isomers (*E* : *Z* = 1 : 1.1).

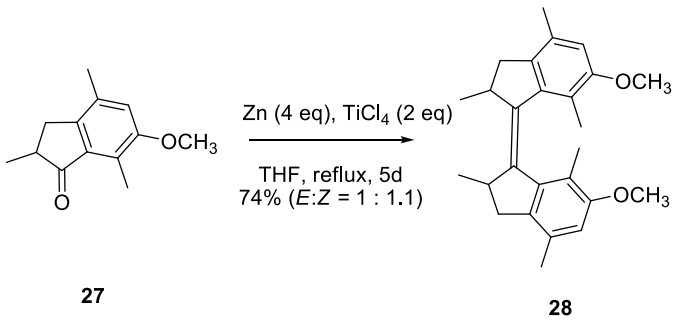

Figure IV.4 Synthesis of bismethoxy molecular motor (**28**)

Both *E* and *Z* isomers of bismethoxy motor (**28**) were characterized by melting point determination, ^{1}H and ^{13}C NMR, as well as HRMS (see Experimental Section). The *E* isomer of **28** has higher melting point than the *Z* isomer probably due to more compact packing in its crystal structure. The mass of each isomer corresponded to that calculated for the protonated molecule $[M + H]^{+}$ employing electrospray ionization (ESI). ^{1}H and ^{13}C NMR data of the corresponding protons and carbons of *E* and *Z* isomers of **28** are presented in **Table IV.1** and **IV.2** respectively. Upon homocoupling to form the central double bond, the ^{13}C NMR signal of the ketone functionality in **27** disappeared and the ^{1}H NMR signal of the aromatic proton experienced an upfield shift (see Experimental Section). The ^{1}H NMR chemical shifts of the two methyl groups of the xylyl moiety in *E*-**28** (**Table IV.1**) are close to each other, whereas in *Z*-**28** (**Table IV.2**), their chemical shifts are quite different. The methyl group that is close to the other xylyl moiety (*fjord* region) in the *Z* isomer experiences a decent upfield shift due to shielding by the adjacent aromatic ring.

Table IV.1 ^{1}H and ^{13}C NMR data of the corresponding protons and carbons of *E*-**28**.

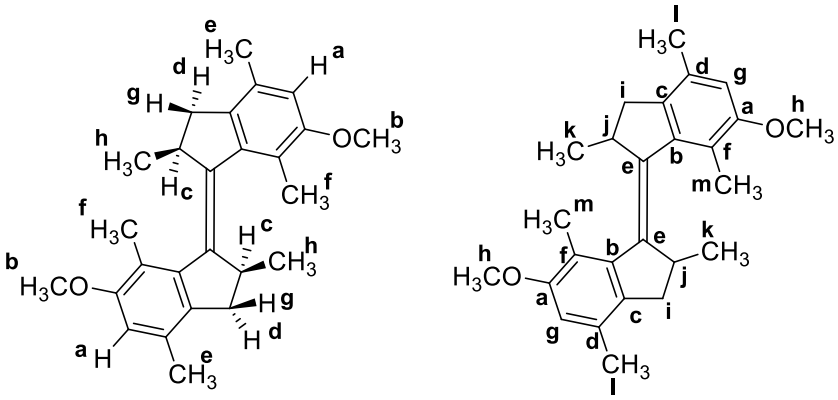

Hydrogen	δ_H (ppm)	Multiplicity	*J* (Hz)	Carbon	δ_C (ppm)
$\mathbf{H_a}$	6.56	*s*	-	$\mathbf{C_a}$	156.9
$\mathbf{H_b}$	3.86	*s*	-	$\mathbf{C_b}$	142.6
$\mathbf{H_c}$	2.86 − 2.93	*m*	-	$\mathbf{C_c}$	141.8
$\mathbf{H_d}$	2.60	*dd*	14.1, 5.7	$\mathbf{C_d}$	134.1
$\mathbf{H_e}$	2.30	*s*	-	$\mathbf{C_e}$	131.4
$\mathbf{H_f}$	2.20	*s*	-	$\mathbf{C_f}$	120.4
$\mathbf{H_g}$	2.16	*d*	14.1	$\mathbf{C_g}$	110.0
$\mathbf{H_h}$	1.09	*d*	6.5	$\mathbf{C_h}$	55.9
				$\mathbf{C_i}$	42.4
				$\mathbf{C_j}$	38.5
				$\mathbf{C_k}$	19.3
				$\mathbf{C_l}$	18.9
				$\mathbf{C_m}$	16.3

Table IV.2 ^{1}H and ^{13}C NMR data of the corresponding protons and carbons of *Z*-**28.**

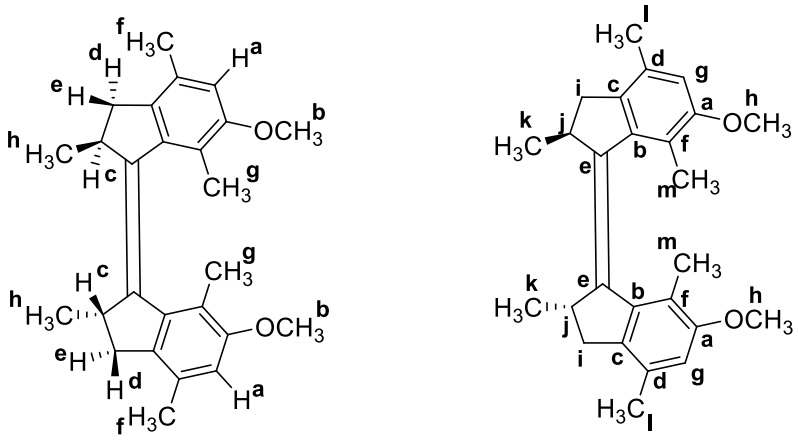

Hydrogen	δ_H (ppm)	Multiplicity	*J* (Hz)	Carbon	δ_C (ppm)
$\mathbf{H_a}$	6.53	*s*	-	$\mathbf{C_a}$	156.5
$\mathbf{H_b}$	3.78	*s*	-	$\mathbf{C_b}$	142.2
$\mathbf{H_c}$	3.30 – 3.36	*m*	-	$\mathbf{C_c}$	141.1
$\mathbf{H_d}$	3.05	*dd*	14.5, 6.4	$\mathbf{C_d}$	136.0
$\mathbf{H_e}$	2.38	*d*	14.5	$\mathbf{C_e}$	130.5
$\mathbf{H_f}$	2.26	*s*	-	$\mathbf{C_f}$	122.1
$\mathbf{H_g}$	1.37	*s*	-	$\mathbf{C_g}$	110.3
$\mathbf{H_h}$	1.07	*d*	6.8	$\mathbf{C_h}$	55.9
				$\mathbf{C_i}$	42.0
				$\mathbf{C_j}$	38.2
				$\mathbf{C_k}$	20.6
				$\mathbf{C_l}$	19.0
				$\mathbf{C_m}$	14.4

The mechanism of the McMurry homocoupling depends strongly on the reducing agent used in the reaction. Using Zn, a relative weak reducing agent, it is believed that the active species is a low-valent Ti(II) species. The indanone (**27**) forms a complex with the active Ti(II) species leading to the formation of double bond via a

mechanism similar to pinacol radical-radical coupling reaction[88]. The proposed reaction pathway of the synthesis of bismethoxy molecular motor (**28**) is shown in **Figure IV.5**.

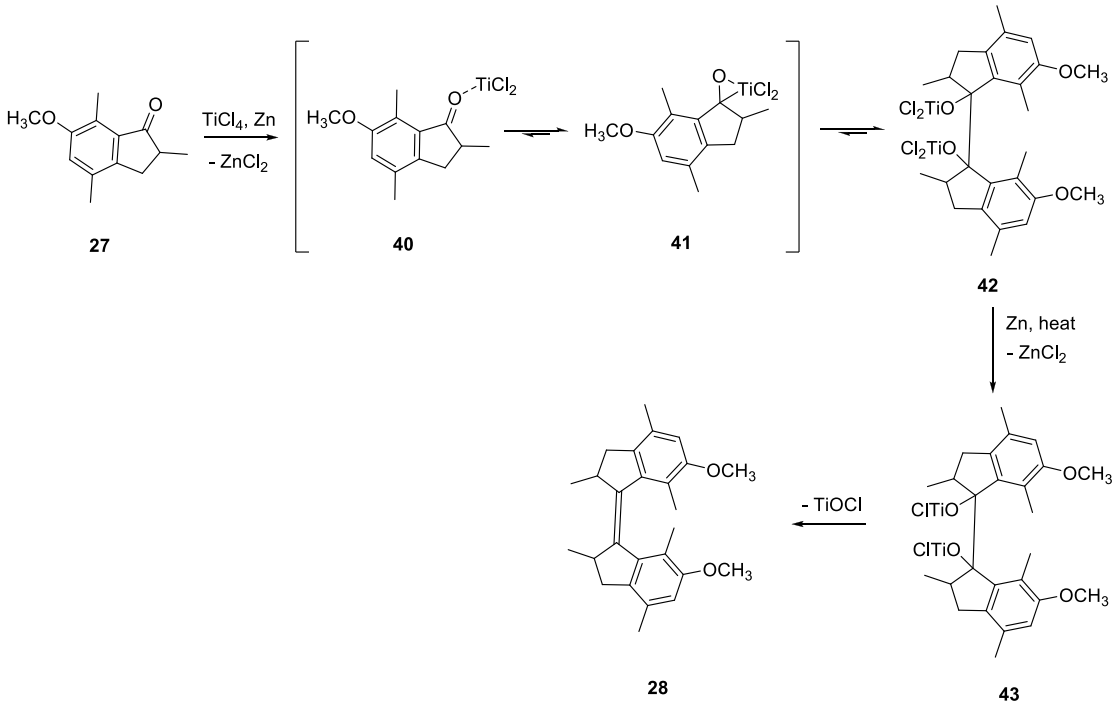

Figure IV.5 Proposed reaction pathway of the synthesis of bismethoxy molecular motor (**28**)

The final step in the synthesis of biphenol molecular motor (**M1**) is the deprotection of the two methoxy groups in **28** to give the phenol moieties. The deprotection was achieved by heating a mixture of **28** and 6 equivalents of CH_3MgI at 160 ℃ for 16 hours under N_2 atmosphere (**Figure IV.6**). A needle was equipped to allow the evaporation of the solvent along with the gas formed during the reaction. Upon acidic work-up with saturated NH_4Cl solution, the biphenol molecular motor (**M1**) was obtained in 61% yield as the *Z* isomer. The interesting thing is that the yield of the *Z* isomer which was more than 50% despite the fact that the starting material (**28**) was an approximately 1:1 mixture of *E* and *Z* isomers. A possible explanation for this result is that the *E* isomer underwent thermal isomerization to form more

thermodynamically stable *Z* isomer during the deprotection reaction at such high temperature. It is supported by the change of the ratio of *E* and *Z* isomers in the crude product after the reaction to favor the *Z* isomer (*E* : *Z* = 1 : 3.6). However, the thermal *E*-*Z* isomerization process has not been fully investigated yet. The biphenol molecular motor (**M1**) was characterized by ^{1}H and ^{13}C NMR spectroscopy as well as HRMS (see Experimental Section). Melting point of **M1** could not be determined due to degradation of the compound. The mass of the biphenol molecular motor (**M1**) corresponded to that calculated for the protonated molecule $[M + H]^{+}$ employing atmospheric pressure chemical ionization (APCI). ^{1}H and ^{13}C NMR spectra of **M1** showed some signals similar to those of *Z*-**28** (**Table IV.2**), except the disappearance of the methoxy protons and the appearance of the hydroxyl protons as a singlet broad peak ($\delta_H = 4.48$ ppm). The disappearance of the methoxy groups was also confirmed by ^{13}C NMR spectroscopy and HRMS.

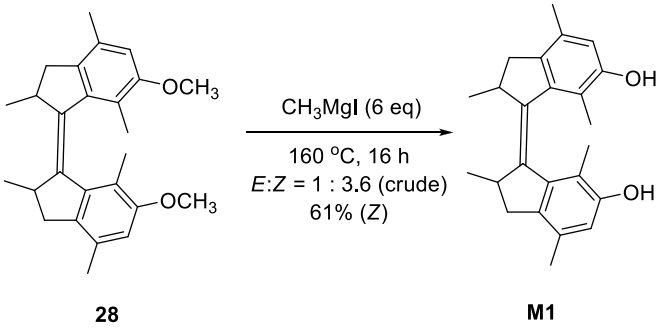

Figure IV.6 Deprotection of bismethoxy molecular motor (**28**)

The proposed mechanism of the deprotection of bismethoxy molecular motor (**28**) is depicted in **Figure IV.7**. The methyl anion of the Grignard reagent (CH_3MgI) is thought to attack the carbon atom of the methoxy groups to generate the phenolate anions (**44** and **45**) and ethane gas (C_2H_6) as the side product. Upon acidic work-up, the phenolate anions are protonated to give the biphenol molecular motor (**M1**). Although an excess of the Grignard reagent had been used in the reaction, the mono-deprotected product (**46**) was still observed during the purification by column chromatography.

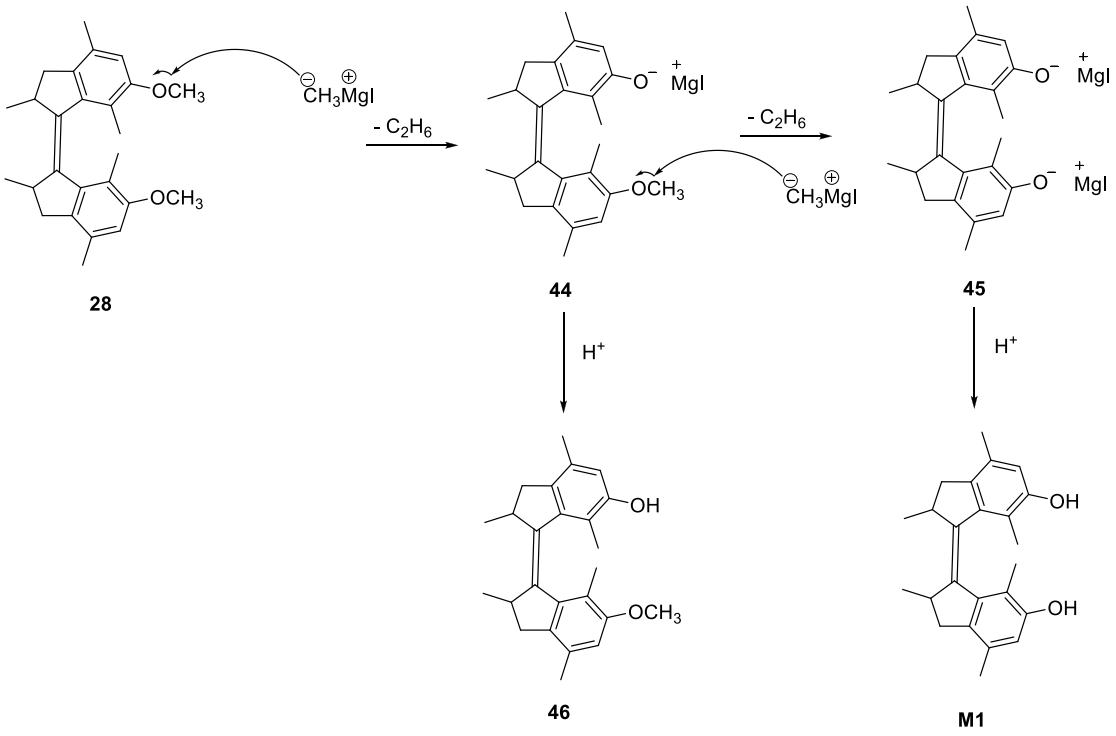

Figure IV.7 Proposed mechanism of the deprotection of bismethoxy molecular motor (**28**)

IV.1.2 Resolution of biphenol molecular motor (M1)

The biphenol molecular motor (**M1**) obtained from the synthesis was a racemic mixture of its two enantiomers. Both enantiopure isomers can be obtained by means of separation from their mixture through resolution. In this research, both enantiomers of **M1** were resolved by employing (8*S*,9*R*)-*N*-benzylcinchonidinium chloride as the resolving agent in two different solvents (acetonitrile and EtOAc) as shown in **Figure IV.8**. The enantiopure cinchona alkaloid formed a diastereomeric complex with one of the **M1** enantiomers through chiral recognition. Interestingly, the solvent had an important role in determining which **M1** enantiomer that formed the diastereomeric complex with the resolving agent. In EtOAc, the resolving agent favored the formation of the diastereomeric complex with (*R,R*)-**M1**, whereas in acetonitrile, the formation of the diastereomeric complex with (*S,S*)-**M1** was more favorable. Further study on the effect of solvent in the formation of the

diastereomeric complex between **M1** and the resolving agent is still under investigation in our group.

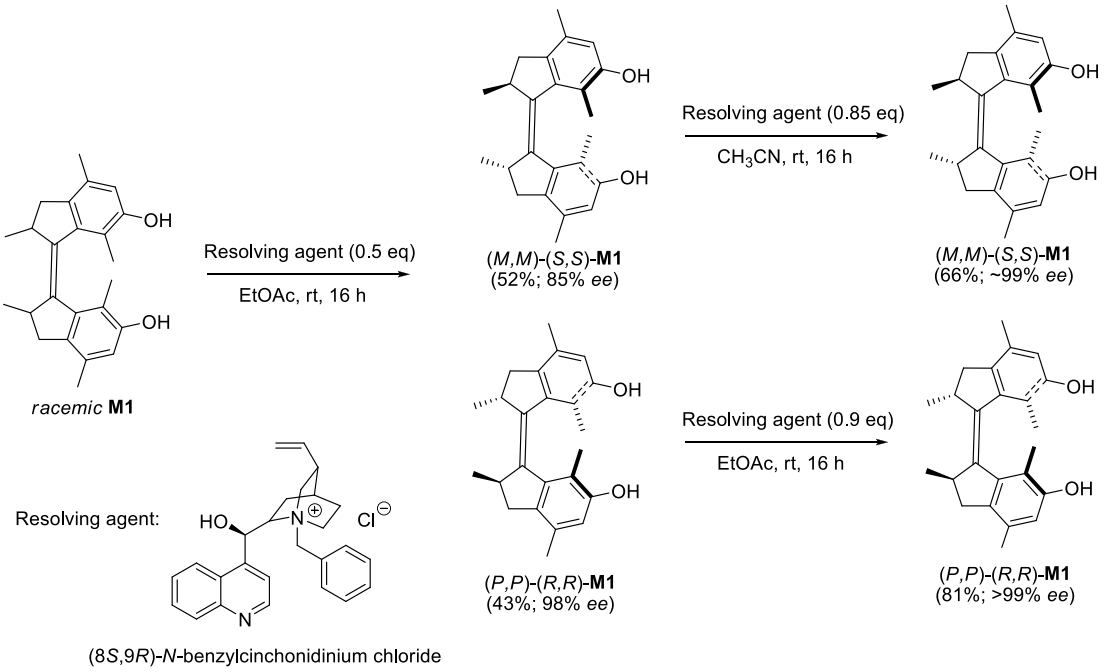

Figure IV.8 Resolution of biphenol molecular motor (**M1**)

In the first resolution, the resolving agent formed the diastereomeric complex with (*R,R*)-**M1** in EtOAc. The amount of the resolving agent used was 0.5 equivalent to prevent the formation of diastereomeric complex with (*S,S*)-**M1**. The diastereomeric complex of (*R,R*)-**M1** was then separated from (*S,S*)-**M1** by means of filtration. After acidic work-up to re-convert the complex to the starting enantiomer, (*R,R*)-**M1** was obtained in 43% recovery and 98% *ee*, whereas the (*S,S*)-**M1** was obtained in 52% recovery and 85% *ee*. The recovery of the (*S,S*) enantiomer, which was more than 50%, was reasonable judging from its enantiomeric excess (*ee*), which was lower than the (*R,R*) enantiomer. It is because there was still a little bit of unresolved (*R,R*)-**M1** left as impurity causing higher recovery and lower *ee*. The second resolution was performed to amplify the *ee* of both enantiomers obtained from the first resolution. The (*R,R*)-**M1** was resolved using the same procedure as the previous resolution,

except the amount of the resolving agent was increased to increase the recovery of the product. After the second resolution, (*R,R*)-**M1** was obtained as an enantiomerically pure (>99% *ee*) compound in 81% recovery. On the other hand, the (*S,S*)-**M1** was resolved using acetonitrile as the solvent to prefer the formation of its diastereomeric complex with the resolving agent. After the second resolution, (*S,S*)-**M1** was obtained as a nearly enantiomerically pure (~99% *ee*) compound in 66% recovery.

Apart from the determination of their enantiomeric excess (*ee*), both enantiomers of **M1** were also characterized by UV-Vis and circular dichroism (CD) spectroscopy as well as optical rotation measurement. Both **M1** enantiomers have the exact same UV-Vis spectra as shown in **Figure IV.9a**. However, their absorption in the CD spectra (**Figure IV.9b**) show the opposite signs to each other (opposite Cotton effect) which prove that they are enantiomers. The observation in the CD spectra is also supported by the optical rotations of both enantiomers which are opposite to each other (see Experimental Section).

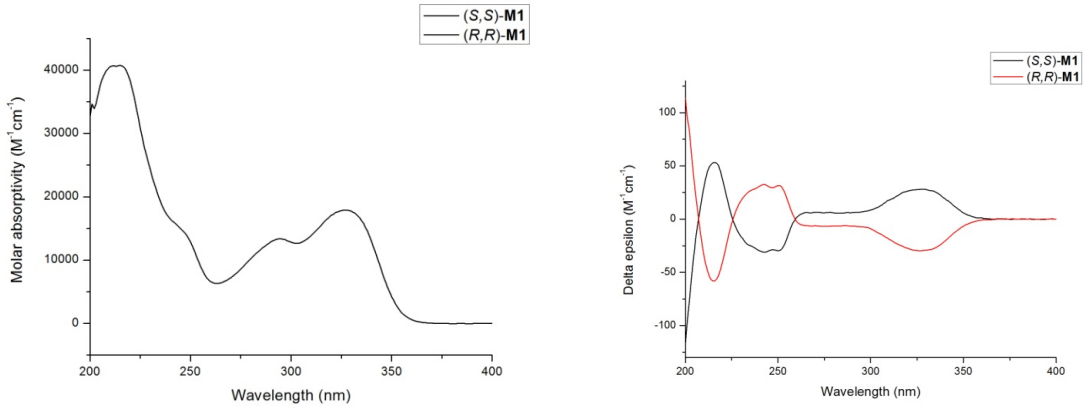

a **b**

Figure IV.9 UV-Vis (a) and CD (b) spectra of both enantiomers of **M1**

IV.2 Synthesis of Biaryls (L1 − L4)

The conformationally flexible biaryls used in this research are 3,3'-bipyridine (**L1**), 4,4'-biisoquinoline (**L2**), and two 4,4'-biisoquinoline derivatives, namely 1,1'-dimethyl-4,4'-biisoquinoline (**L3**) and 1,1'-diphenyl-4,4'-biisoquinoline (**L4**). Each

of the four biaryls was synthesized in one reaction step according to literature procedures[64,83,85].

IV.2.1 Synthesis of 3,3'-bipyridine (L1)

3,3'-Bipyridine (**L1**) was synthesized using a Pd-catalyzed cross coupling reaction of pyridine (**47**) and 3-bromopyridine (**48**) as reported in literature[83] (**Figure IV.10**). This reaction is a C3-selective arylation of pyridine employing a catalyst generated *in situ* from $Pd(OAc)_2$ and 1,10-phenantroline (Phen). Cs_2CO_3 was found to be an effective inorganic base in the reaction[83]. Upon heating the reaction mixture at 140 ℃ for 3 days, the reaction went to full conversion and gave 3,3'-bipyridine (**L1**) in 42% yield as yellow oil. The product was characterized by ^1H and ^{13}C NMR spectroscopy as well as HRMS (see Experimental Section). ^1H NMR spectrum of **L1** showed four aromatic proton signals which corresponded to those reported in the literature[83]. ^{13}C NMR spectrum of **L1** showed five sp^2-hybridized carbon signals which corresponded to the carbons of the aromatic rings. The mass of **L1** obtained from HRMS also corresponded to that calculated for the protonated molecule $[M + H]^+$ employing electrospray ionization (ESI).

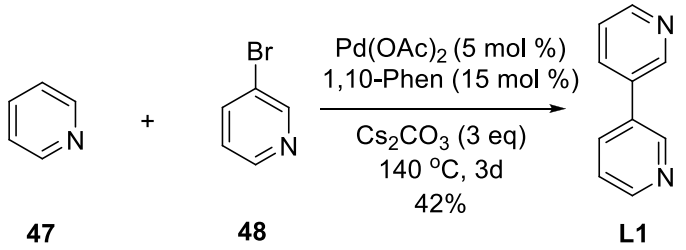

Figure IV.10 Synthesis of 3,3'-bipyridine (**L1**)

The plausible mechanism of this reaction as proposed in the literature[83] is shown in **Figure IV.11**. The first step in the catalytic cycle is the coordination of pyridine ring (**47**) to the Pd centre of the catalyst through N atom (**50**). Due to the strong bidentate coordination of the Phen ligand, the N-bound pyridine substrate will be destabilized and then dissociates from Pd center. Subsequently, the pyridine substrate will reorients itself to bind to Pd through a π system (**51**) which triggers the selective

C3-H activation to form the aryl-Pd(II) species (**53**). Oxidative addition of 3-bromopyridine (**48**) to this intermediate (**53**) followed by reductive elimination gives **L1** as the desired product[83]. The catalyst (**49**) is regenerated by ligand exchange mediated by Cs_2CO_3 to complete the catalytic cycle.

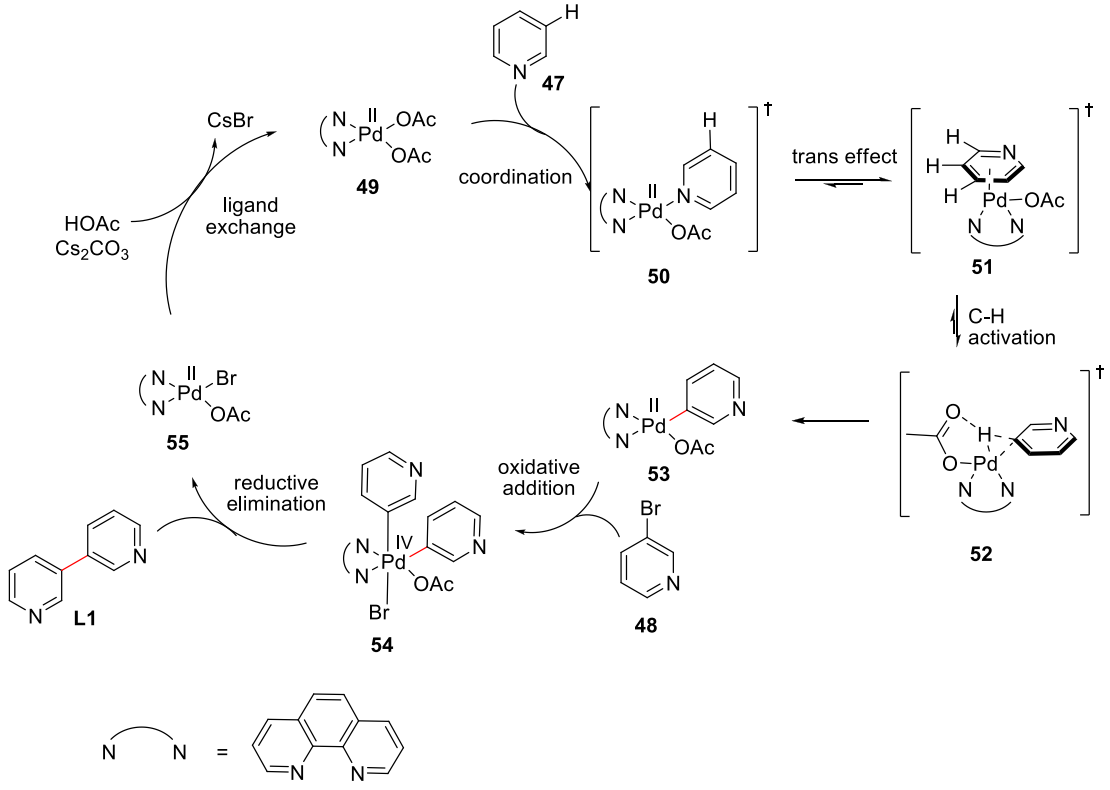

Figure IV.11 Plausible mechanism of the synthesis of 3,3'-bipyridine (**L1**)

IV.2.2 Synthesis of 4,4'-biisoquinoline (L2)

The synthesis of 4,4'-biisoquinoline (**L2**) was achieved via a Ni-catalyzed homocoupling reaction of 4-bromoisoquinoline (**56**) according to literature procedure[64] (**Figure IV.12**). The reaction involved *in situ* formation of $Ni^0(PPh_3)_3$ from the reduction of $NiCl_2(PPh_3)_2$ by Zn^0 powder. Et_4NI was added as an electrolyte to facilitate the redox reaction. $Ni^0(PPh_3)_3$ generated in this fashion was suitable for the homocoupling of aryl halides[64,89]. After heating at 50 ℃ for 3 days, the reaction went to full conversion, but only gave **L2** in 5% yield. This low yield is comparable

to that reported in literature (13%)[64]. The low yield could be caused by the side reaction which involved phenyl transfer from PPh_3 ligand[89]. This hypothesis was supported by the isolation of the side product which had more aromatic protons than those expected from **L2** in the ^1H NMR spectrum. The target product (**L2**) was characterized by melting point determination, ^1H and ^{13}C NMR spectroscopy as well as HRMS (see Experimental Section). ^1H NMR spectrum of **L2** showed six aromatic proton signals which corresponded to those reported in the literature[64]. ^{13}C NMR spectrum of **L2** showed seven sp^2-hybridized carbon signals which corresponded to the carbons of the aromatic rings. The mass of **L2** obtained from HRMS also corresponded to that calculated for the protonated molecule $[M + H]^+$ employing electrospray ionization (ESI).

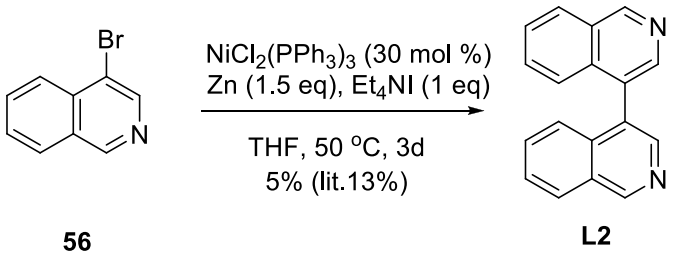

Figure IV.12 Synthesis of 4,4'-biisoquinoline (**L2**)

Several reaction mechanisms have been proposed for the Ni-catalyzed coupling of aryl halides. One of the mechanism involves Ni(I) and Ni(III) species as the intermediates[89,90]. **Figure IV.13** shows one of the proposed mechanism of the Ni-catalyzed homocoupling of 4-bromoisoquinoline (**56**). The first step is the oxidative addition of the aryl halide (**56**) to the Ni(0) catalyst (**57**) to generate Ni(II) species (**58**). The next step is the Zn-mediated reduction of **58** to Ni(I) species (**59**). Oxidative addition of the second aryl halide (**56**) to **59** generates the Ni(III) species (**60**). Reductive elimination of **60** gives 4,4'-biisoquinoline (**L2**) as the product and Ni(I) species (**61**) which is then reduced by Zn to recover the Ni(0) catalyst (**57**).

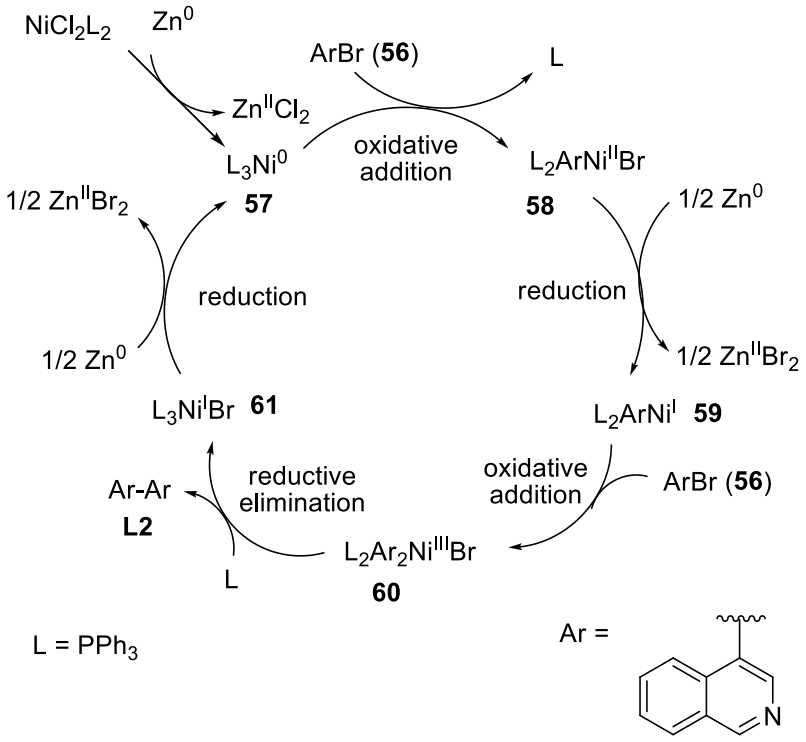

Figure IV.13 Proposed mechanism of the synthesis of 4,4'-biisoquinoline (**L2**)

IV.2.3 Synthesis of 4,4'-biisoquinoline derivatives (L3 and L4)

Two 4,4'-biisoquinoline derivatives which have methyl (**L3**) and phenyl (**L4**) substituents at 1 and 1' positions were synthesized via 1,4-functionalization of isoquinoline (**62**) using MeLi and PhLi respectively as reported in the literature[85] (**Figure IV.14**). These reactions involved nucleophilic addition to isoquinoline (**62**) by the organolithium reagents at 1-position followed by electrophilic trapping with C_2Cl_6 at 4-position. 1,2-dimethoxyethane (DME) was added to accelerate the reaction of the organolithium reagents with isoquinoline (**62**) and allow electrophilic trapping before rearomatization[85]. However, in our reactions, the electrophile (C_2Cl_6) was added very slowly to the reaction mixture to allow the formation of the dimer structure as desired in our target products (**L3** and **L4**). Upon quenching with MeOH and aromatization by means of oxidation, both reactions went to full conversion and gave **L3** and **L4** in 27% and 49% yield respectively. Complete aromatization of **L3**

required addition of DDQ (2,3-dichloro-5,6-dicyano-*p*-benzoquinone) as an oxidizing agent, whereas **L4** achieved complete aromatization upon exposure to air[85].

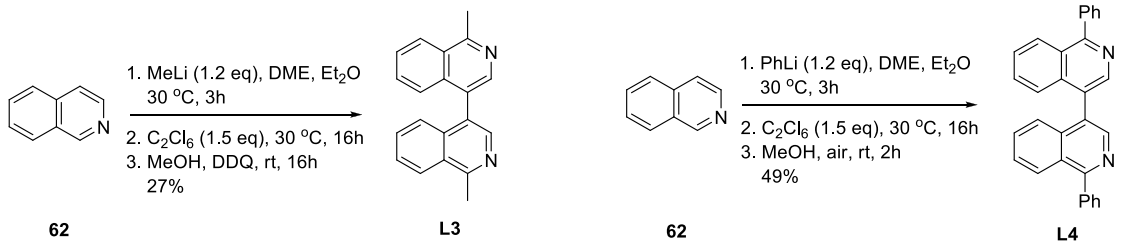

Figure IV.14 Synthesis of 4,4'-biisoquinoline derivatives (**L3** and **L4**)

Both 4,4'-biisoquinoline derivatives (**L3** and **L4**) were characterized by melting point determination, ^{1}H and ^{13}C NMR spectroscopy as well as HRMS (see Experimental Section). ^{1}H NMR spectrum of **L3** showed five aromatic proton signals and one methyl proton signal. ^{13}C NMR spectrum of **L3** showed nine sp^2-hybridized carbon signals which corresponded to the carbons of the aromatic rings and one methyl carbon signal. Both ^{1}H and ^{13}C NMR data of **L3** corresponded to those previously reported in the literature[85]. ^{1}H NMR spectrum of **L4** showed only four aromatic proton signals due to the overlap of some signals. ^{13}C NMR spectrum of **L4** showed 13 sp^2-hybridized carbon signals which corresponded to the carbons of the isoquinoline and phenyl rings. The mass of both **L3** and **L4** obtained from HRMS corresponded to those calculated for the protonated molecules $[M + H]^+$ employing electrospray ionization (ESI).

The proposed mechanism of the synthesis of **L3** and **L4** via 1,4-functionalization is depicted in **Figure IV.15**. The first step is the nucleophilic addition of methyl/ phenyl anion of the organolithium reagents at 1-position of isoquinoline (**62**) which subsequently generates anion at N atom (**63N**) or C4-position (**63C**). The dihydro intermediate (**63C**) is then trapped by C_2Cl_6 as the electrophile. The resulting product (**64**) is thought to undergo further reaction with the remaining anion intermediate (**63C**) to form the dimer structure (**65**). The target product (**L3**/ **L4**) is obtained upon oxidation/ aromatization of **65**[85].

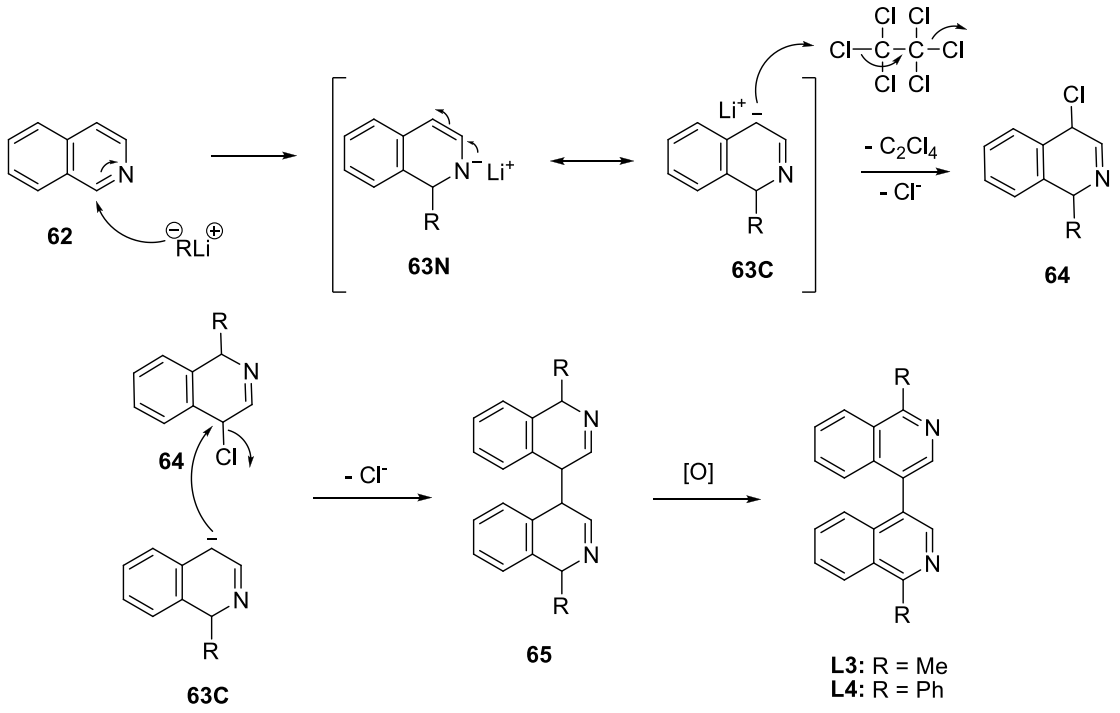

Figure IV.15 Proposed mechanism of synthesis of 4,4'-biisoquinoline derivatives (**L3** and **L4**)

IV.3 Study on Photochemical and Thermal Isomerization of Bismethoxy Motor (28)

In order to verify that **28** operates as molecular motor which can undergo unidirectional rotation (**Figure IV.16**), the photochemical and thermal isomerization steps of **28** were studied in a MeOH solution using UV-Vis and ^{1}H NMR spectroscopy.

The first isomerization step is the photoisomerization of *E*-stable **28** to generate *Z*-unstable **28** (**Figure IV.16** step 1). This process was monitored by means of UV-Vis spectroscopy (**Figure IV.17**). Irradiation of a solution of *E*-stable **28** with UV light (λ_{max} = 312 nm) at 20 ℃ led to a significant red-shift of the major absorption band centered at 286 nm to a new absorption band centered at 352 nm. The red-shift which was also observed for the corresponding parent motor without the methoxy substituents[34], was consistent with increased strain on the central double bond in *Z*-

unstable **28**. During the irradiation, two clear isosbestic points (the wavelengths at which the absorbance remained constant) were maintained at 263 nm and 328 nm, indicating that the photoisomerization of *E*-stable **28** to *Z*-unstable **28** proceeded without any signs of degradation of the compounds.

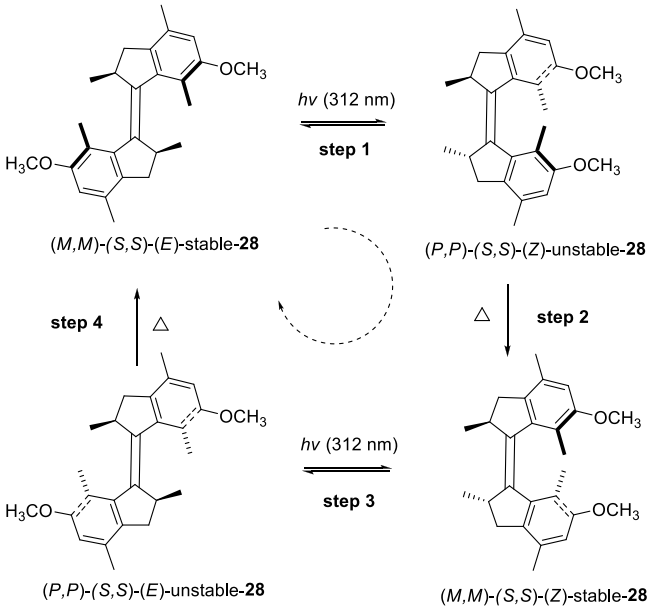

Figure IV.16 Photochemical and thermal isomerization steps of bismethoxy motor (**28**) leading to 360° unidirectional rotation

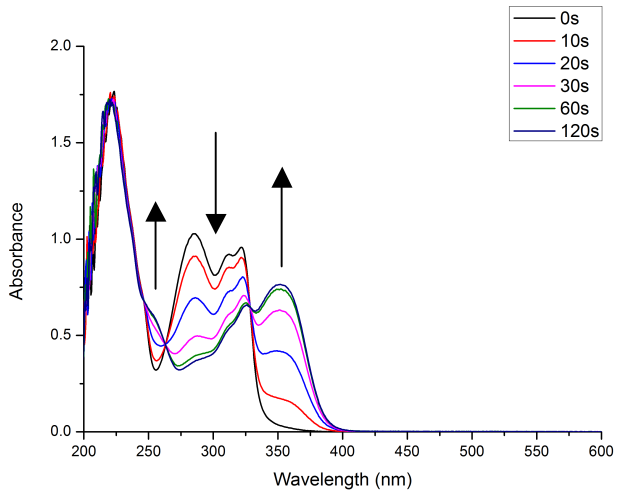

Figure IV.17 Change in the UV-Vis absorption spectra of *E*-stable **28** (c = 5.47 x 10^{-5} M in MeOH) at 20 °C upon irradiation with UV light at 312 nm

Apart from UV-Vis spectroscopy, the photoisomerization of *E*-stable **28** to generate *Z*-unstable **28** was also studied by means of ^{1}H NMR spectroscopy. Upon irradiation of *E*-stable **28** in CD_3OD at 25 ℃, some new signals appeared in the ^{1}H NMR spectrum which corresponded to the protons of *Z*-unstable **28** (**Figure IV.18 a → b**; see Experimental Section for peak assignments). When compared to the proton signals of *E*-stable **28** (**Figure IV.18a**), the proton signal of the stereogenic methyl groups (protons Ha) in *Z*-unstable **28** (**Figure IV.18b**) experienced a downfield shift from 1.08 ppm to 1.48 ppm due to the conformational change from the preferred axial to the disfavored equatorial orientation upon photoisomerization. Another significant shift was the signal of methyl protons of the xylyl moieties at the *fjord* region (protons Hb) which experienced an upfield shift from 2.19 ppm to 1.22 ppm due to shielding by the adjacent aromatic ring. The methoxy protons (protons Hc) experienced a slight shift in the same way as protons Hb due to the same reason. Since the *E*-*Z* photosiomerization is a reversible reaction, a mixture of *E*-stable **28** and *Z*-unstable **28** was obtained at the equilibrium. The photostationary state (PSS) ratio was found to be 24 (*E*-stable **28**): 76 (*Z*-unstable **28**) as determined by relative integration of their ^{1}H NMR signals.

The second isomerization step is the thermal helix inversion of *Z*-unstable **28** to generate *Z*-stable **28** (**Figure IV.16** step 2). This process was monitored by means of ^{1}H NMR spectroscopy. Upon heating the PSS mixture of *E*-stable **28** and *Z*-unstable **28** at 50 ℃ for 16 h, the signals of the unstable form disappeared and some new peaks corresponded to the protons of *Z*-stable **28** were observed (**Figure IV.18 b → c**). Upon thermal helix inversion, the proton signal of the stereogenic methyl groups (protons Ha) in *Z*-stable **28** (**Figure IV.18c**) shifted back to that similar to *E*-stable **28** (1.07 ppm) due to the change in conformation to adopt the preferred axial orientation again. Furthermore, the thermodynamic parameters of activation ($\Delta H^{\ddagger}$, $\Delta S^{\ddagger}$, $\Delta G^{\ddagger}$) for this process were determined by kinetic analysis of this process at five different temperatures (35, 40, 45, 50, 55 ℃). The thermal isomerization was followed by monitoring the change in the UV-Vis absorbance (in MeOH) at 360 nm as a function

of time. Using the Eyring equation (**Figure IV.19**), it was determined that the thermal helix inversion of *Z*-unstable **28** to *Z*-stable **28** has an entalphy of activation ($\Delta H^{\ddagger}$) of (89.3 ± 1.9) kJ mol^{-1}, entropy of activation ($\Delta S^{\ddagger}$) of – (30.5 ± 6.1) J K^{-1} mol^{-1}. The calculated Gibbs free energy of activation ($\Delta G^{\ddagger}$) for this process at 20 °C is (98.2 ± 0.2) kJ mol^{-1} which corresponds to the half life ($t_{1/2}$) of (9.95 ± 0.66) h at the same temperature.

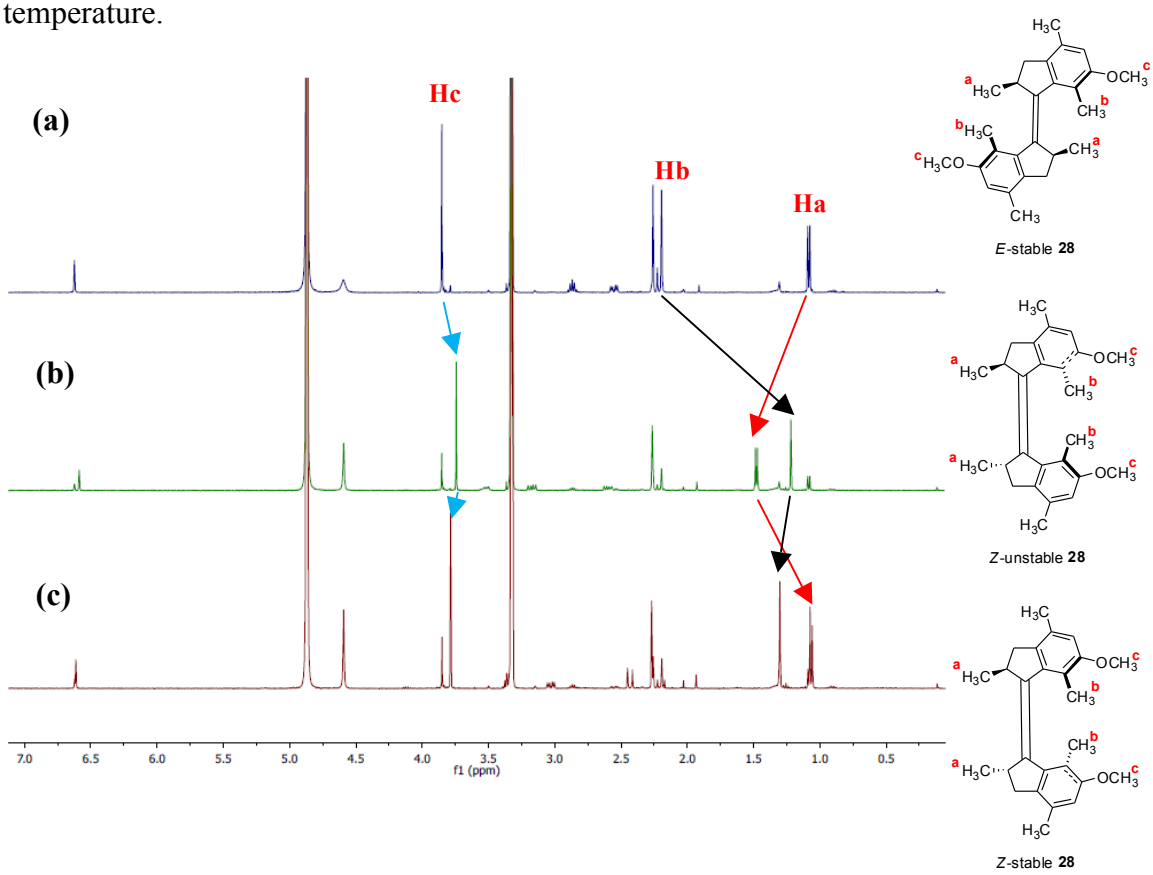

Figure IV.18 ^{1}H NMR spectra (400 MHz, CD_3OD, 25 °C) of (a) *E*-stable **28**, (b) *Z*-unstable **28** formed upon UV irradiation to PSS, and (c) *Z*-stable **28** obtained after thermal isomerization of *Z*-unstable **28** at 50 °C

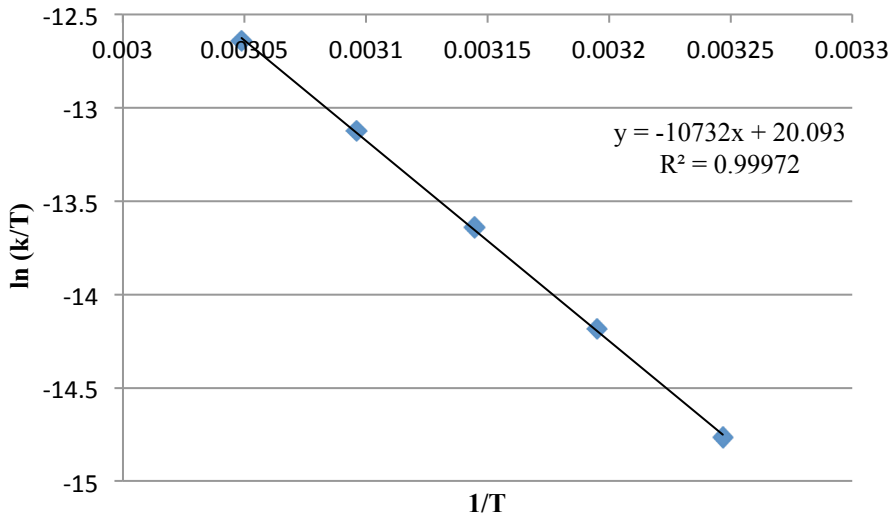

Figure IV.19 Eyring plot for the thermal helix inversion of *Z*-unstable **28** to *Z*-stable **28** in MeOH

The third isomerization step is the photoisomerization of *Z*-stable **28** to generate *E*-unstable **28** (**Figure IV.16** step 3). This process, like the first step, was also monitored by means of UV-Vis spectroscopy (**Figure IV.20**). Irradiation of a solution of *Z*-stable **28** with UV light (λ_{max} = 312 nm) at -25 °C led to a slight red-shift of the major absorption band centered at 322 nm to a new absorption band centered at 335 nm. The red-shift which was also observed for the corresponding parent motor[34], indicated the formation of *E*-unstable **28** which had higher torsional strain on the central double bond. During the irradiation, three isosbestic points were maintained at 253 nm, 263 nm and 326 nm respectively, indicating that the photoisomerization of *Z*-stable **28** to *E*-unstable **28** proceeded without any degradation of the compounds. The isosbestic points were not clearly observed due to the low temperature used in the measurement to prevent the following thermal isomerization step generating *E*-stable **28**.

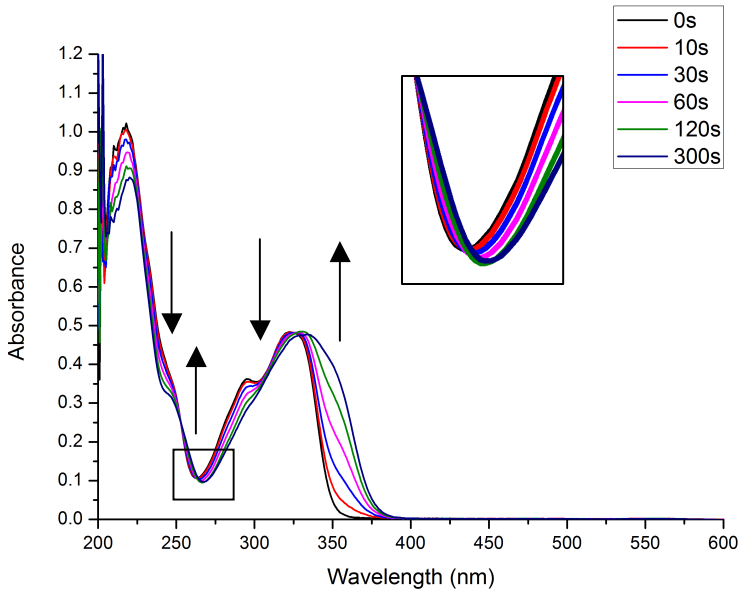

Figure IV.20 Change in the UV-Vis absorption spectra of *Z*-stable **28** (c = 2.12 x 10^{-5} M in MeOH) at -25 ℃ upon irradiation with UV light at 312 nm

In addition to UV-Vis spectroscopy, the photoisomerization of *Z*-stable **28** to generate *E*-unstable **28** was also studied by means of ^{1}H NMR spectroscopy. Upon irradiation of *Z*-stable **28** in CD_3OD at -60 ℃, some new signals appeared in the ^{1}H NMR spectrum (recorded at -35 ℃) which corresponded to the protons of *E*-unstable **28** (**Figure IV.21 a → b**; see Experimental Section for peak assignments). The irradiation and ^{1}H NMR measurement were performed at low temperatures to prevent the following thermal helix inversion of *E*-unstable **28** to generate *E*-stable **28** which occurred rapidly at room temperature. When compared to the proton signals of *Z*-stable **28** (**Figure IV.21a**), the proton signal of the stereogenic methyl groups (protons Ha) in *E*-unstable **28** (**Figure IV.21b**) experienced an upfield shift from 1.04 ppm to 0.78 ppm due to the shielding by the adjacent aromatic ring in spite of the conformational change from the preferred axial to the disfavored equatorial orientation upon photoisomerization. Another significant shift was the signal of methyl protons of the xylyl moieties at the *fjord* region (protons Hb) which is no longer shielded by the adjacent aromatic ring resulting in a downfield shift from 1.28

ppm to 1.97 ppm. The methoxy protons (protons Hc) experienced a slight shift in the same way as protons Hb due to the same reason. Similar to the *E*-*Z* photosiomerization in the first step, a mixture of *Z*-stable **28** and *E*-unstable **28** was obtained at the equilibrium. The photostationary state (PSS) ratio was found to be 33 (*Z*-stable **28**): 67 (*Z*-unstable **28**) as determined by relative integration of their ^{1}H NMR signals.

The final isomerization step is the thermal helix inversion of *E*-unstable **28** to generate the starting *E*-stable **28** to complete the 360° rotary cycle (**Figure IV.16** step 4). This process was monitored by means of ^{1}H NMR spectroscopy. Upon warming the PSS mixture of *Z*-stable **28** and *E*-unstable **28** to 25 ℃, the signals of the unstable form disappeared and some new peaks corresponding to the protons of *E*-stable **28** were observed (**Figure IV.21 b → c**). Upon thermal helix inversion, the proton signal of the stereogenic methyl groups (protons Ha) in *E*-stable **28** (**Figure IV.21c**) shifted back to that similar to *Z*-stable **28** (1.05 ppm) due to the change in conformation to adopt the preferred axial orientation again. Furthermore, the thermodynamic parameters of activation ($\Delta H^{\ddagger}$, $\Delta S^{\ddagger}$, $\Delta G^{\ddagger}$) for this process were determined by kinetic analysis of this process at six different temperatures (-25, -22.5, -20, -17.5, -15, -10 ℃). The thermal isomerization was followed by monitoring the change in the UV-Vis absorbance (in MeOH) at 360 nm as a function of time. Using the Eyring equation (**Figure IV.22**), it was determined that the thermal helix inversion of *E*-unstable **28** to *E*-stable **28** has an entalphy of activation ($\Delta H^{\ddagger}$) of (71.0 ± 1.0) kJ mol^{-1}, entropy of activation ($\Delta S^{\ddagger}$) of – (19.7 ± 4.0) J K^{-1} mol^{-1}. The calculated Gibbs free energy of activation ($\Delta G^{\ddagger}$) for this process at 20 ℃ is (76.8 ± 0.2) kJ mol^{-1} which corresponds to the half life ($t_{1/2}$) of (5.48 ± 0.35) s at the same temperature. The Gibbs free energy of activation ($\Delta G^{\ddagger}$) for both thermal helix inversion steps (**Figure IV.16** step 2 and 4) of bismethoxy motor (**28**) are close to those reported for the parent motor[34,91], indicating that the introduction of the methoxy group does not have a significant influence on the thermal isomerization steps.

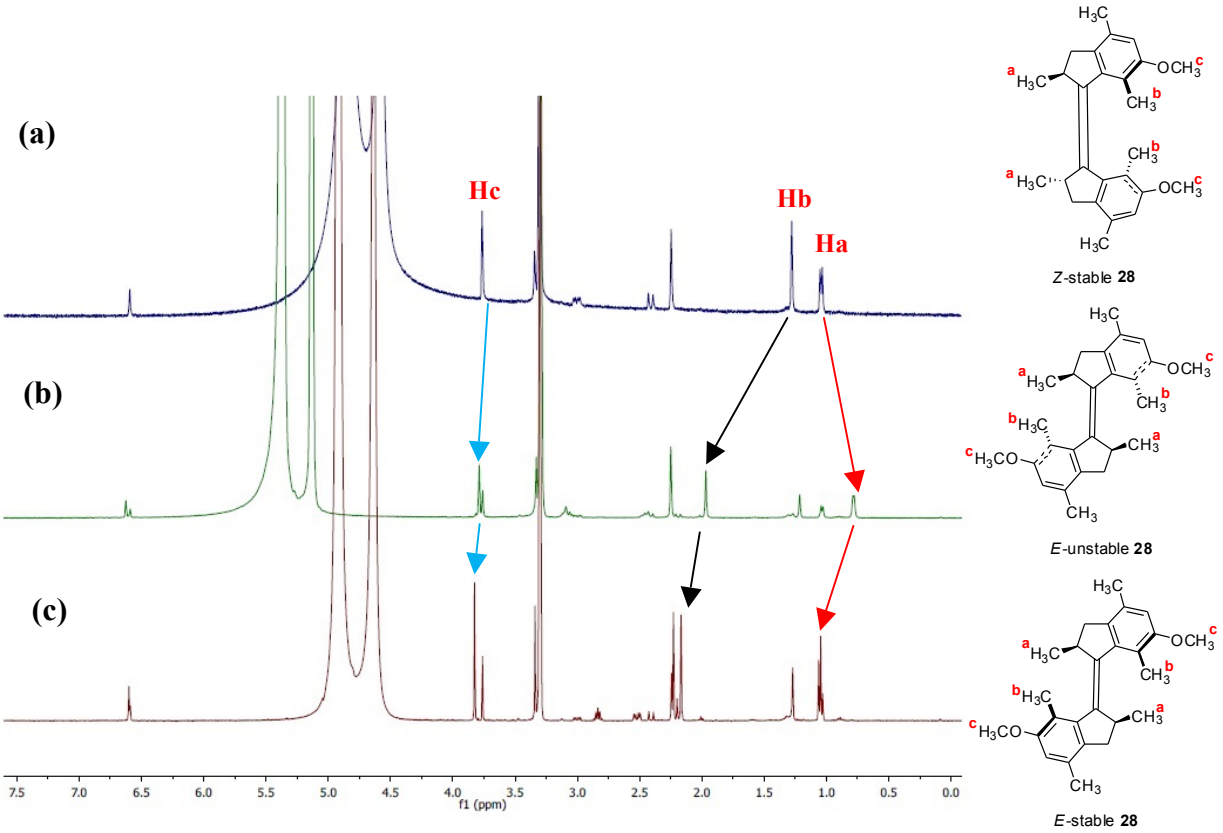

Figure IV.21 ^{1}H NMR spectra [400 MHz, CD_3OD, 25 °C (a,c)/ -35 °C (b)] of (a) *Z*-stable **28**, (b) *E*-unstable **28** formed upon UV irradiation to PSS, and (c) *E*-stable **28** obtained after thermal isomerization of *Z*-unstable **28** at 25 °C

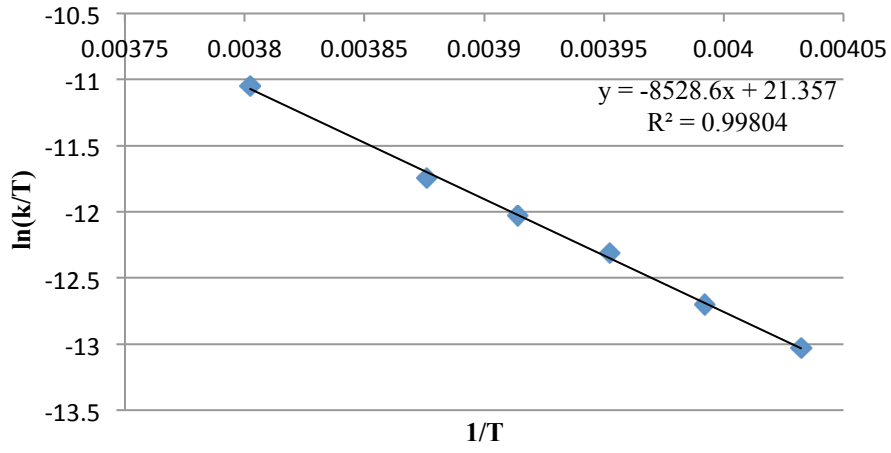

Figure IV.22 Eyring plot for thermal helix inversion of *E*-unstable **28** to *E*-stable **28** in MeOH

IV.4 Binding Study of Biphenol Motor (M1) with 3,3'-Bipyridine (L1), 4,4'-Biisoquinoline (L2), and (*S,S*)-*N,N'*-Dimethyl-1,2-cyclohexanediamine (L5)

The transfer of chirality from our biphenol molecular motor (**M1**) to the biaryls (**L1**−**L4**) is supposed to occur via the formation of their complexes through hydrogen bonding (**Figure I.5a**). As a preliminary study, we tried to determine the binding constant of the motor (**M1**) with 3,3'-bipyridine (**L1**) as well as 4,4'-biisoquinoline (**L2**) by means of ^{1}H NMR spectroscopy. The binding study was carried out by analyzing the chemical shifts of the peaks in ^{1}H NMR spectra upon a series of dilution of the 1:1 mixture. The experiment was generally performed in aprotic solvents, such as hexane and toluene[13] to prevent hydrogen bonding of the compounds with the solvent. Upon complexation, it was expected that there were some new peaks in the ^{1}H NMR spectra corresponded to the complex of the motor (**M1**) and the biaryls (**L1**/ **L2**), which would undergo shifts as the concentration decreased due to less association of **M1** and **L1**/ **L2**.

Figure IV.23 shows the ^{1}H NMR spectra of 1:1 mixture of **M1** and **L1** in CD_2Cl_2 at different concentrations compared to pure **M1** and the expected hydrogen bonding between **M1** and **L1**. Initially, we attempted to make a solution of the complex in less polar solvent (toluene) hoping to get stronger hydrogen bonding between **M1** and **L1**. Unfortunately, it was unsuccessful due to the low solubility of **M1** in toluene. Even in moderately polar solvent, such as CD_2Cl_2, the maximum concentration achieved for the complex was relatively low (0.03 M). In the ^{1}H NMR spectra shown in **Figure IV.23**, one can observe that there are no other significant shifts of the proton signals except the hydroxyl proton signal of **M1** (indicated by arrow) upon dilution of the 1:1 mixture of **M1** and **L1**. The upfield shift of the hydroxyl proton signal could be caused by hydrogen bonding with residual water content in CD_2Cl_2 solvent. This explanation was supported by the observed shift of the residual water proton signal (δ_H ~ 1.60 ppm) in the ^{1}H NMR spectra. In order to overcome the influence of water in the hydrogen bonding of **M1** and **L1**, the dilution experiment was redone using

anhydrous $CDCl_3$ purchased from commercial supplier. However, to our disappointment, similar result was obtained in which only the hydroxyl proton signal of **M1** shifted upon dilution of the 1:1 mixture. A possible explanation for this is there was no expected hydrogen bonding between the motor (**M1**) and 3,3'-bipyridine (**L1**) as shown in **Figure IV.23**. Instead, they probably formed some random hydrogen bonds with each other which resulted only in the shift of the hydroxyl proton signal.

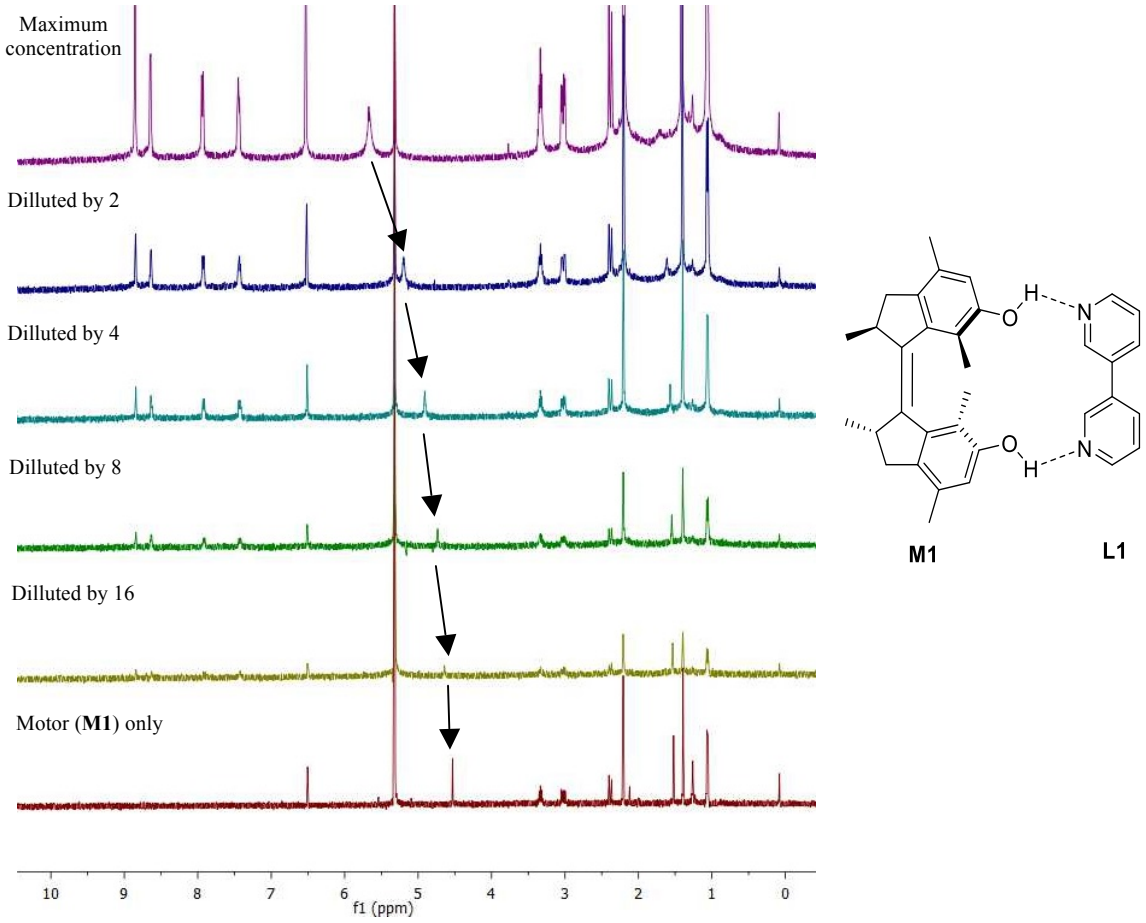

Figure IV.23 ^{1}H NMR spectra (400 MHz, CD_2Cl_2, 25 ℃) of 1:1 mixture of **M1** and **L1** (*c* max = 0.03 M) upon a series of dilution compared to pure **M1** (left) and the expected hydrogen bonding between **M1** and **L1** (right)

Furthermore, study on the binding of biphenol molecular motor (**M1**) with 4,4'-biisoquinoline (**L2**) was also performed using the same method as previously

described for 3,3'-bipyridine (**L1**). The ^{1}H NMR spectra of 1:1 mixture of **M1** and **L2** in CD_2Cl_2 upon a series of dilution compared to pure **M1** and the expected hydrogen bonding between **M1** and **L2** are shown in **Figure IV.24**. The maximum concentration achieved for this complex in CD_2Cl_2 was even lower (0.012 M) than the complex of **M1** and **L1**. Unfortunately, there are also no other significant shifts observed in the ^{1}H NMR spectra (**Figure IV.24**) except the hydroxyl proton signal of **M1** (indicated by arrow). It is probably due to hydrogen bonding with residual water content in CD_2Cl_2 solvent as supported by the shift of the residual water proton signal (δ_H ~ 1.60 ppm). This result also indicates that there was no expected hydrogen bonding between **M1** and **L2** as shown in **Figure IV.24**.

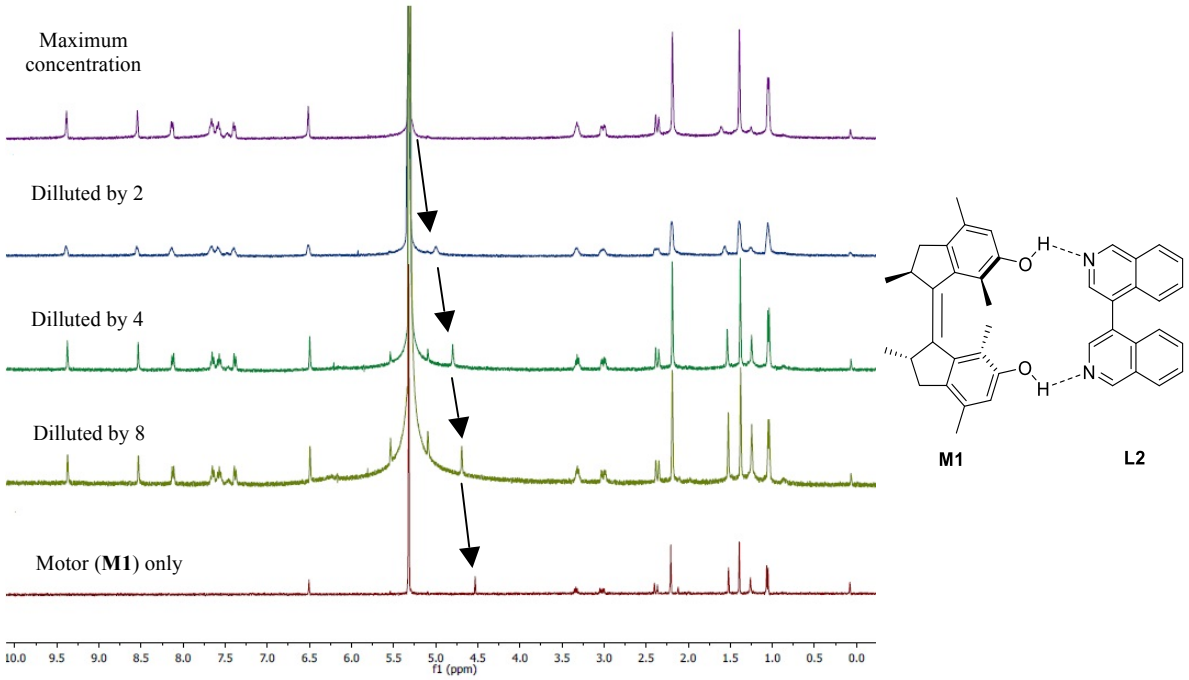

Figure IV.24 ^{1}H NMR spectra (400 MHz, CD_2Cl_2, 25 ℃) of 1:1 mixture of **M1** and **L2** (*c* max = 0.012 M) upon a series of dilution compared to pure **M1** (left) and the expected hydrogen bonding between **M1** and **L2** (right)

In addition to the two biaryls (**L1** and **L2**), study on the binding of the biphenol motor (**M1**) with a chiral diamine (**L5**) as a potential switchable chiral receptor (**Figure I.5b**) was also performed on the basis of which reported in the literature[13] for

biphenol system. The binding study of **M1** with (*S,S*)-*N,N'*-dimethyl-1,2-cyclohexanediamine (**L5**) was carried out by analyzing the chemical shifts of the peaks in ^{1}H NMR spectrum of the 1:1 mixture (0.03 M in $CDCl_3$) compared to the peaks in ^{1}H NMR spectra of each pure compound (**Figure IV.25**). The experiment was performed twice, in $CDCl_3$ dried over anhydrous $MgSO_4$ and commercially purchased anhydrous $CDCl_3$. Unfortunately, both of them showed the same result in which no significant shift was observed for the proton signals of the complex in its ^{1}H NMR spectrum compared to those of pure **M1** and **L5**. This result again indicates that there was no binding between our motor (**M1**) and the chiral diamine (**L5**). A possible explanation for this is the difference in geometry between our motor (**M1**) and the biphenol used in the literature[13]. The two hydroxyl groups in the biphenol are in proximity with each other[13] which may be required for the hydrogen bonding with the diamine, whereas in the motor (**M1**), they are far apart from each other due to the steric overcrowding around the central double bond. Another factor that can also influence the binding is the pK_a value of the phenol moiety. The biphenol used in the literature[13] has nitro substituents at the *ortho* position that can change the pK_a value to obtain stronger hydrogen bonding with the diamine, whereas our motor (**M1**) does not have any nitro substituents resulting in the difference of pK_a value between them.

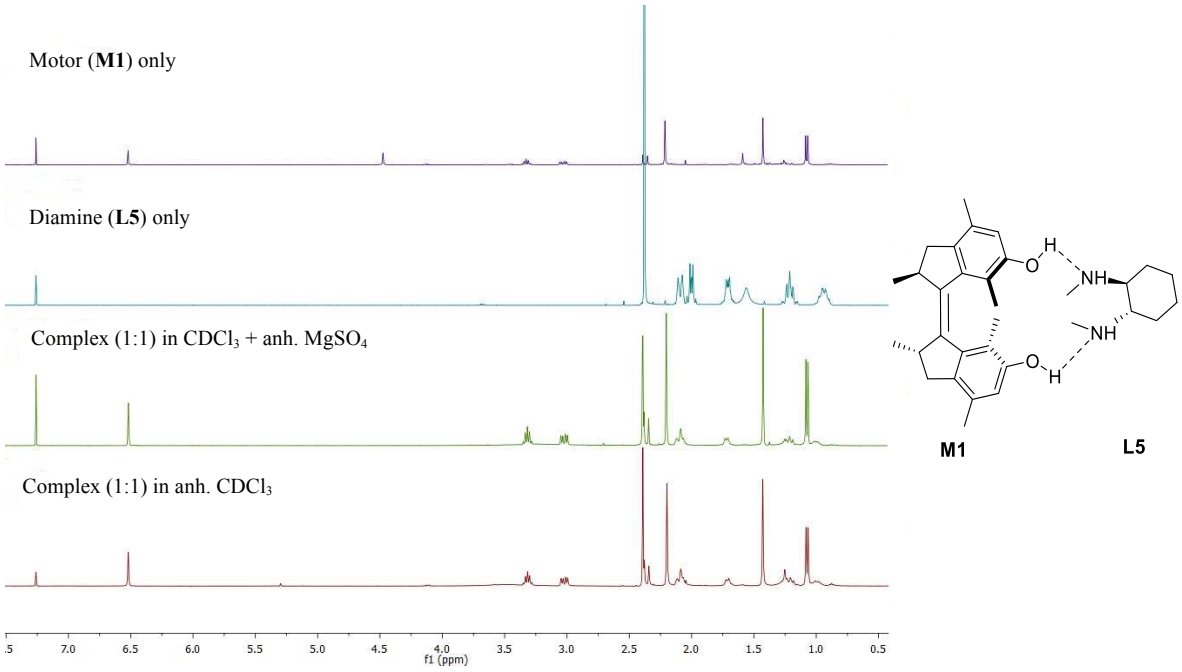

Figure IV.25 ^{1}H NMR spectra (400 MHz, $CDCl_3$, 25 °C) of 1:1 mixture of **M1** and **L5** (c = 0.03 M) compared to each pure compound (left) and the expected hydrogen bonding between **M1** and **L5** (right)

IV.5 Synthesis of Pyridine Molecular Motor Analog (66)

Apart from hydrogen bonding, we also proposed a new design of complex for chirality transfer via coordination bonds to a metal ion employing a pyridine-based molecular motor (**M2**) as depicted in **Figure I.5c**. Initially, we studied the synthesis of the motor (**M2**) using an analog without the methyl substituent on the pyridine ring (**66**). Synthesis of the pyridine molecular motor analog (**66**) can be achieved in four reaction steps based on the retrosynthetic analysis shown in **Figure IV.26**. Similar to the biphenol motor (**M1**), the central double bond in **66** can be introduced by McMurry homocoupling of the corresponding indanone precursor (**67**). The indanone ring can be made from cyclization of the corresponding α,β-unsaturated ketone moiety (**30**) which is the product of nucleophilic addition of isopropenyl magnesium bromide to the Weinreb amide precursor (**29**). The amide functionality can be introduced by functional group interconversion of nicotinic acid (**68**) as the starting material.

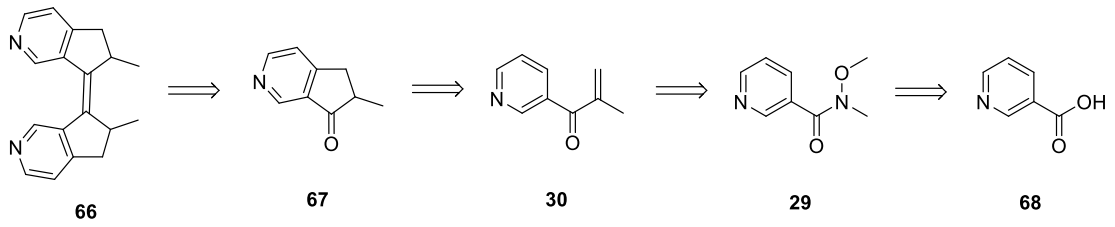

Figure IV.26 Retrosynthetic analysis of pyridine molecular motor analog (**66**)

The first step in the synthesis of pyridine molecular motor analog (**66**) is the synthesis of Weinreb nicotinamide (**29**) from nicotinic acid (**68**) via the formation of acid chloride (**Figure IV.27**). Nicotinic acid (**68**) was converted to its acid chloride using oxalyl chloride $(COCl)_2$ catalyzed by *N,N*-dimethylformamide (DMF) in dichloromethane (DCM). Without isolating the intermediate, the reaction proceeded to the formation of the Weinreb amide (**29**) upon addition of *N,O*-dimethylhydroxylamine hydrochloride and triethylamine (Et_3N). After stirring at room temperature for 16 h, the reaction went to full conversion and gave **29** in good yield (76% over two steps). The product was characterized by ^1H and ^{13}C NMR spectroscopy as well as HRMS (see Experimental Section). ^1H NMR spectrum of **29** showed four aromatic proton signals which corresponded to the protons of the pyridine ring and two aliphatic proton signals that corresponded to the protons of the two methyl groups. The signal of the methoxy protons (OCH_3) showed a more downfield shift than those of the *N*-methyl protons. It is because oxygen is more electronegative than nitrogen causing the methoxy protons to be more deshielded than the *N*-methyl protons. ^{13}C NMR spectrum of **29** showed a typical carbonyl signal of the amide (δ_C = 167.0 ppm), five other sp^2-hybridized carbon signals which corresponded to the carbons of the pyridine ring, and two sp^3-hybridized carbon signals that corresponded to the methyl groups. Both ^1H and ^{13}C NMR data of **29** corresponded to those previously reported in the literature[92]. The mass of **29** obtained from HRMS also corresponded to that calculated for the protonated molecule $[M + H]^+$ employing electrospray ionization (ESI).

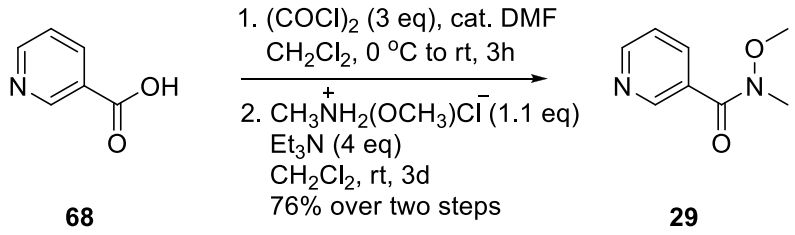

Figure IV.27 Synthesis of Weinreb nicotinamide (**29**)

The proposed mechanism for the synthesis of the Weinreb amide (**29**) is shown in **Figure IV.28**. The first reaction is the acylation of nicotinic acid (**68**) using oxalyl chloride and catalytic DMF. The oxalyl chloride reacts with the DMF to produce an imidoyl chloride derivative (**72**) which is a highly electrophilic cationic intermediate together with CO and CO_2 as the by-products. The next step is the nucleophilic attack of nicotinic acid (**68**) to the C=N bond of the reactive intermediate (**72**) releasing a chloride ion. The chloride ion (Cl^-) then acts as a nucleophile in the nucleophilic substitution at the carbonyl group (**74**) via a tetrahedral intermediate (**75**) to give the acid chloride (**76**) and regenerate the DMF catalyst[93]. The second reaction is simply the nucleophilic substitution of Cl atom in the acid chloride (**76**) with *N,O*-dimethylhydroxylamine (**78**), which is generated upon deprotonation of its salt (**77**) by Et_3N, to give the Weinreb amide (**29**) as the final product.

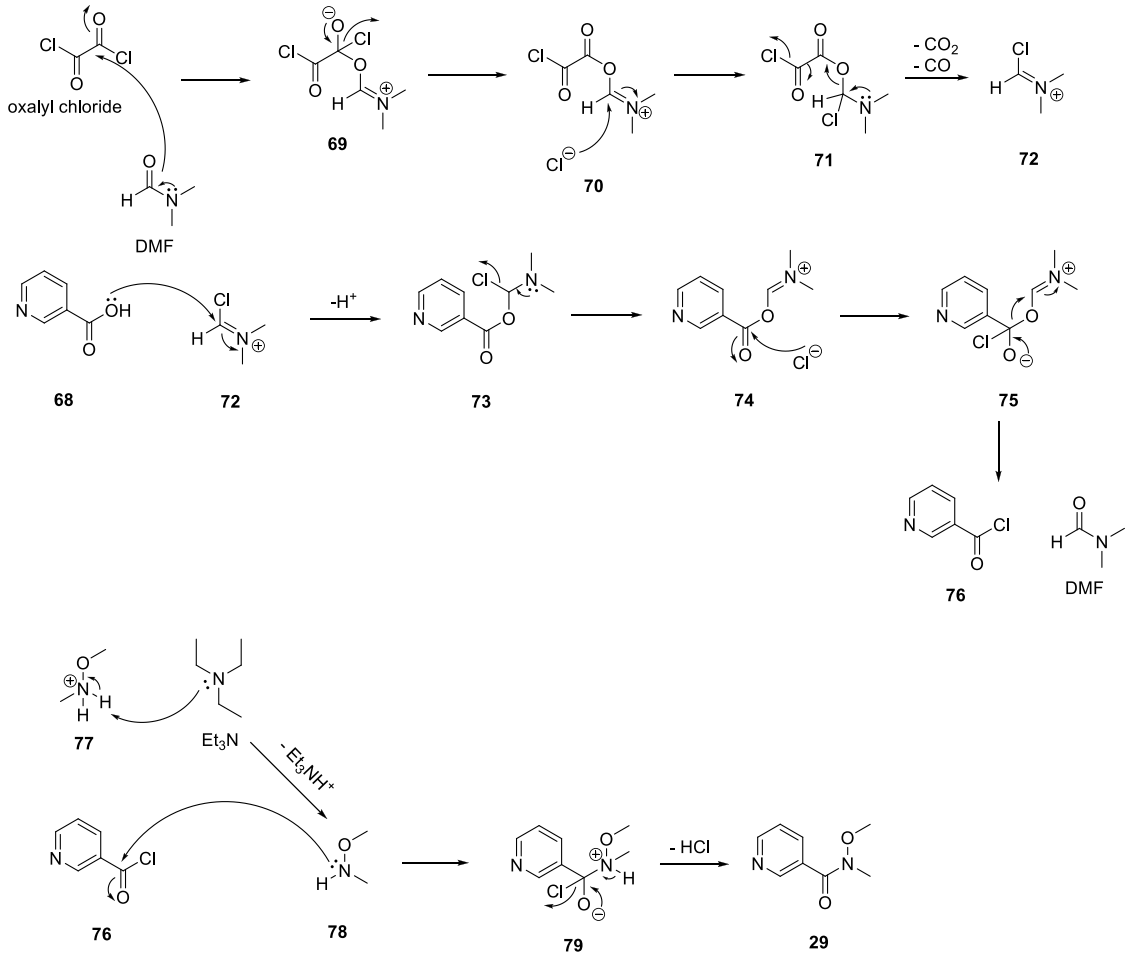

Figure IV.28 Proposed mechanism of the synthesis of Weinreb nicotinamide (**29**) via the formation of acid chloride (**76**)

The second step is the synthesis of the α,β-unsaturated ketone (**30**) by nucleophilic addition of isopropenyl magnesium bromide to the Weinreb amide (**29**) precursor as depicted in **Figure IV.29**. The best result for the reaction was achieved using 3 equivalents of the Grignard reagent at room temperature as reported in the literature[87]. Upon stirring the reaction mixture for 30 minutes at room temperature followed by acidic work-up, the reaction went to full conversion and gave **30** in 41% yield. The reaction was performed in a short time to prevent further reaction of the ketone (**30**) with second equivalent of the Grignard reagent leading to the formation of the over-addition product (alcohol). The target product (**30**) was characterized by

^{1}H and ^{13}C NMR spectroscopy as well as HRMS (see Experimental Section). Upon conversion to the unsaturated ketone (**30**), the ^{1}H and ^{13}C NMR signals of the methoxy and *N*-methyl groups in **29** disappeared and new signals corresponded to the double bond of the isopropenyl moiety in **30** appeared. The ^{13}C NMR signal of the carbonyl functionality (C=O) underwent a downfield shift due to functional group interconversion from amide (**29**) to ketone (**30**). The mass of **30** obtained from HRMS corresponded to that calculated for the protonated molecule $[M + H]^{+}$ employing electrospray ionization (ESI).

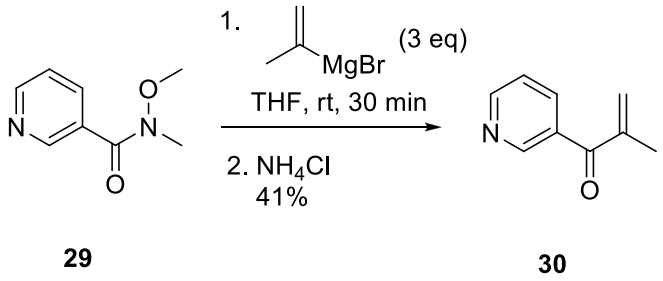

29 **30**

Figure IV.29 Nucleophilic addition of isopropenyl magnesium bromide to Weinreb amide (**29**)

The proposed mechanism for the nucleophilic addition of isopropenyl magnesium bromide (**80**) to the Weinreb amide (**29**) is shown in **Figure IV.30**. The isopropenyl anion of the Grignard reagent (**30**) attacks the carbonyl group of **29** resulting in the formation of a tetrahedral intermediate (**81**). Weinreb amide functionality was chosen as the precursor to synthesize the corresponding ketone due to its high selectivity compared to other carbonyl groups, such as carboxylic acid, ester, and acyl halide which tend to undergo second addition of the Grignard reagent to form an alcohol. The high selectivity of Weinreb amide to form ketone is due to the suggestion that the tetrahedral intermediate (**81**) formed as a result of nucleophilic addition of the Grignard reagent (**80**) is stabilized by chelation with the methoxy group at low temperature[94]. Upon acidic work-up, the intermediate goes to the formation of the unsaturated ketone (**30**) as the target product.

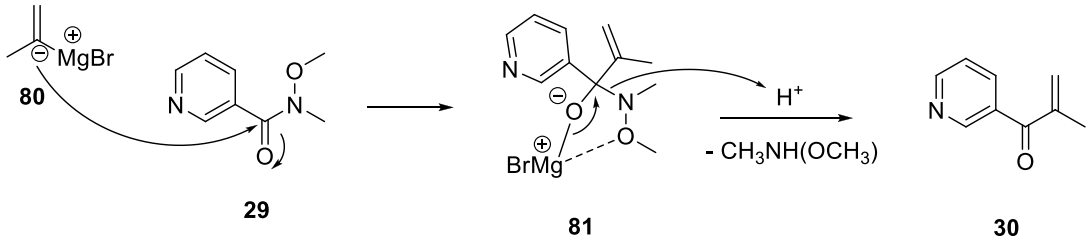

Figure IV.30 Proposed mechanism of the nucleophilic addition of isopropenyl magnesium bromide to Weinreb amide (**29**)

The next step in the synthesis of **66** is the intramolecular cyclization of the unsaturated ketone (**30**) to form the indanone ring (**67**). A common method used for intramolecular cyclization to form the cyclopentenone moiety is the Nazarov cyclization which is an acid-catalyzed 4π conrotatory electrocyclic reaction[95]. Based on this, some test reactions were performed to attempt the Nazarov cyclization of **30** to form the indanone (**67**) employing both Brønsted acids (H_2SO_4, CH_3COOH) and a Lewis acid ($AlCl_3$) as shown in **Figure IV.31**. However, none of these reactions gave the desired product (**67**). The attempted Nazarov cyclization of **30** using H_2SO_4 catalyst led to the formation of a side product which had a mass of [2M – H_2O] as determined by GC-MS employing electron impact (EI) ionization. The side product was likely the product of aldol condensation of our desired product (**67**) to form a dimer structure. The formation of the side product was tried to be suppressed by decreasing the reaction time. Unfortunately, the side product was still formed although the reaction didn't go to full conversion. The reactions employing CH_3COOH and $AlCl_3$ as the acid catalysts led to no conversion of the starting material (**30**). A possible explanation for this is that the acids would first protonate the pyridine ring, making it electron poor which was unfavorable for the Nazarov cyclization to occur. Using an *N*-protected substrate could be the solution to prevent the protonation of the pyridine ring[95]. However, more steps for the protection and deprotection reactions are required which may cause the overall synthesis pathway to be less efficient.

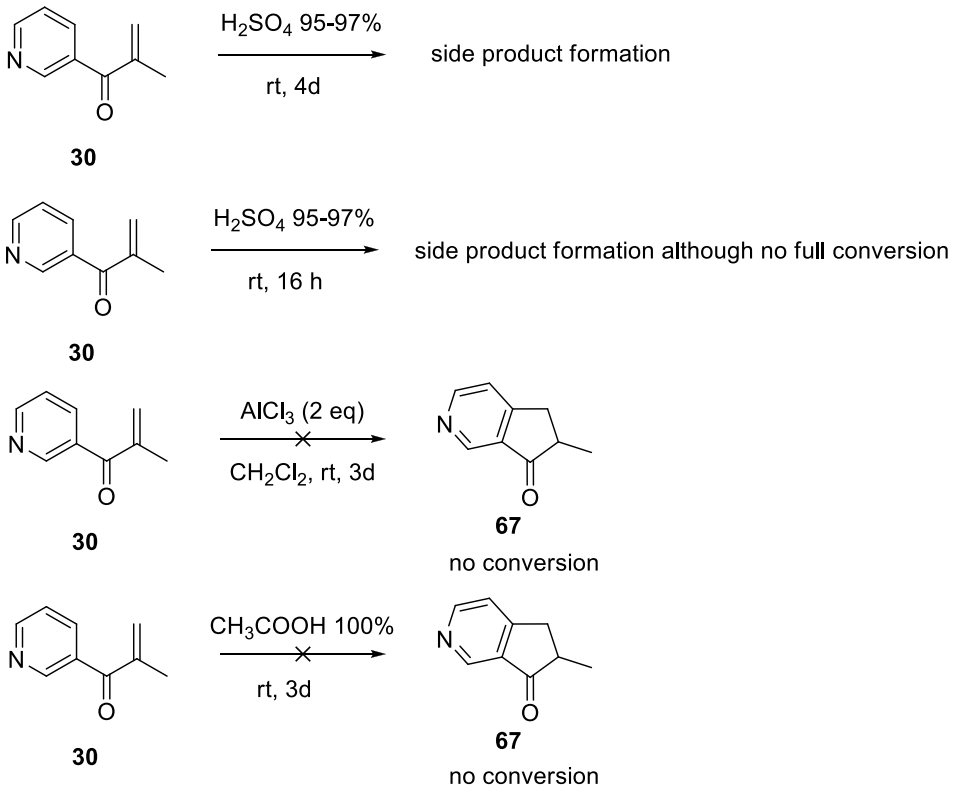

Figure IV.31 Attempted Nazarov cyclization of ketone (**30**) to form indanone (**67**)

Since the Nazarov cyclization didn't give the expected product, we turned to another strategy for the cyclization via *ortho* lithiation. The idea was to introduce a halogen atom, *e.g.* Br, at the desired *ortho* position which would then be used in subsequent intramolecular Heck reaction to form the indanone (**67**). Initially, we studied the *ortho* lithiation of **30** using D_2O as the electrophile (**Figure IV.32**). The reaction was performed employing lithium diisopropylamide (LDA) as the lithiating agent in THF at -78 ℃ and quenched with D_2O. However, ^1H NMR spectrum of the crude product did not show any formation of the desired product (**83**). A possible explanation for this is that the ketone functionality in **30** is not a strong *ortho*-directing group for this reaction. Therefore, we attempted the same reaction using the Weinreb amide (**29**), which was thought to be a stronger *ortho*-directing group than the ketone (**Figure IV.33**). Unfortunately, instead of *ortho*-lithiating at the desired position to form **85**, the Weinreb amide (**29**) underwent the loss of the methoxy group by deprotonation

with LDA to yield amide (**86**). The same result was also obtained for the similar reaction of Weinreb amide with other strong base, such as n-BuLi as reported in the literature[96]. As the *ortho* lithiation pathway also did not yield our target product, the synthesis of the pyridine motor analog (**66**) has yet been unsuccessful to this point.

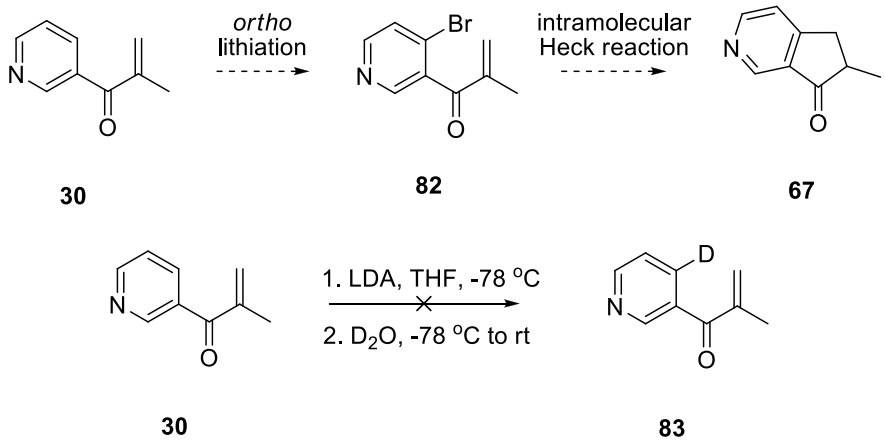

Figure IV.32 Reaction pathway to form indanone (**67**) via *ortho* lithiation of ketone (**30**) (top) and attempted *ortho* lithiation of ketone (**30**) (bottom)

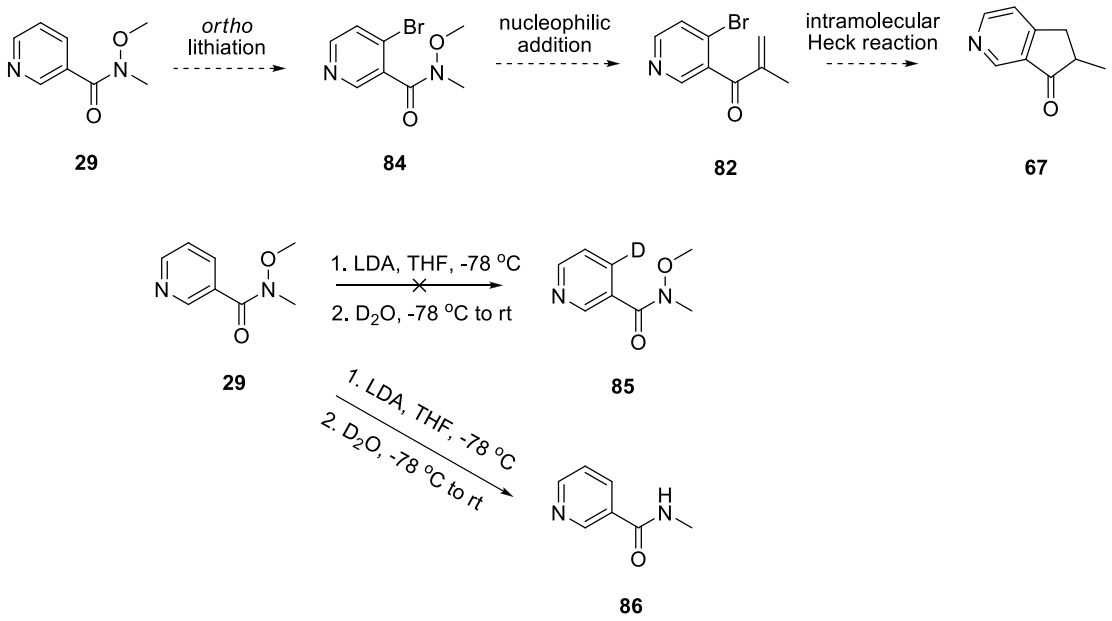

Figure IV.33 Reaction pathway to form indanone (**67**) via *ortho* lithiation of Weinreb amide (**29**) (top) and attempted *ortho* lithiation of Weinreb amide (**29**) (bottom)